Faculty of Science

SRON Netherlands Institute for Space Research

Astrophysics Programme Utrecht

X-ray absorption spectroscopy of the hot interstellar medium near the Galactic center

Bachelor Thesis

M. L. van Gelder

Supervisors:
Dr. T. Prokopec
Institute for Theoretical Physics Utrecht

Dr. E. Costantini
SRON Netherlands Institute for Space Research

January 13, 2016

Abstract

In this thesis, we present a research carried out on the hot phase of the Interstellar Medium (ISM), which is an important tracer of star formation and supernova activity and ultimately of Galaxy evolution. High-resolution X-ray spectroscopy was used to asses the homogeneity and temperature of the hot phase of the ISM near the Galactic center as function of the line of sight. Twelve background X-ray sources were used to attain these properties. An indication of hot gas with a temperature of $\sim 10^7$ K and hydrogen column densities of $\sim 10^{21} - 10^{22}$ cm^{-2} has been detected. This agrees with theoretical expectations. However, the quality of the data did not allow stringent constraints on the gas parameters. We discuss possible factors which influenced our analysis.

Keywords: Galaxy: center — Galaxy: local interstellar matter — X-rays: ISM

Contents

1 Introduction **1**

1.1 X-ray binaries 2

1.2 Collisional ionized equilibrium 4

1.2.1 Ionization rate coefficient 5

1.2.2 Recombination rate coefficient 6

1.3 Absorption Spectra 7

2 Data analysis **9**

2.1 Sample selection 9

2.2 Data conversion 10

2.3 Analysis 11

3 Results **14**

4 Discussion **16**

4.1 Gas intrinsic to the source 19

5 Conclusion **21**

6 Acknowledgements **22**

Appendix A Data Tables **23**

References **27**

1 Introduction

Many astrophysical environments have been observed and studied using X-ray spectroscopy. One of these is the Interstellar Medium (ISM). The ISM consists of a mix of gas and dust, located in between stars. Its structure and composition is regulated by earlier generations of stars, inputting matter and energy into the the ISM [1]. The ISM accounts for about 10-15 % of the mass in the Galactic disk, and can have temperatures varying from cold ($\lesssim 10\,\mathrm{K}$) to hot ($\sim 10^6\,\mathrm{K}$) [2].

Hot gas has been observed in and around the Galaxy [3]. It is an important tracer of star formation and super nova activity. Stars originate from nebulae collapsing under their own gravity, and supernova explosions drastically alter the surrounding ISM by inputting energy and matter into the ISM [4]. Therefore the hot gas ultimately traces galaxy evolution as a function of time since both star formation and supernova activity are tracers of galaxy evolution. By observing various absorption lines (i.e. $\mathrm{O_{VII}}$ Kα, $\mathrm{O_{VII}}$ Kβ & $\mathrm{O_{VIII}}$ Kα) the temperature of the Galactic hot gas was constrained to $\sim 2 \times 10^6\,\mathrm{K}$, and it was seen to have hydrogen column densities of $\sim 10^{19} - 10^{20}\,\mathrm{cm^{-2}}$ [5–7]. The abundances of elements were assumed to be Cosmic, although for oxygen and neon these values may be higher [7].

Observations towards the Galactic center (GC), however, are very difficult because a lot of star formation and supernova activity is going on in this dense region. This makes it difficult to see and derive the physical processes happening in between. Thanks to the high spatial resolution of the *Chandra*-satellite, we can resolve single background sources and thus use the brightest of them for high energy resolution spectral analysis. With about 2 million seconds of observations with *Chandra*, about 4000 discrete X-ray sources had been detected [8], together with a Galactic central diffuse emission with temperatures ranging from $3/4\,\mathrm{keV}$ to $1.5\,\mathrm{keV}$ [6]. A lot of measurements were devoted to the putative Black Hole Sgr A* of the center of the Milky Way. Surrounding hot gas is believed to have a temperature of $\lesssim 10^7\,\mathrm{K}$ [9].

The hot phase of the ISM can be seen in absorption against the spectrum of bright background X-ray sources. The study of the absorption lines in the spectra of these sources allows the determination of both the column density and the temperature of the intervening hot gas.

Through a multiple-source analysis, we want to asses the homogeneity and the temperature of the hot gas near the GC as function of the line of sight (LOS). This temperature will represent an upper limit for the temperature of hot gas in the Galaxy. In the following we will introduce the basic theory of X-ray binaries , collisional ionized equilibrium and absorption spectra in sections 1.1-1.3. In section 2, the sample selection, data reduction, and analysis methods will be explained. The results will be reported in section 3, after which they will be discussed in section 4. Finally, we will draw our conclusions in section 5.

1.1 X-ray binaries

X-ray binaries consist of two stars orbiting each other in a binary system. One of the stars is either a neutron star (NS) or black hole (BH), hereafter called the primary. X-ray binaries are classified according to the mass of the companion star, hereafter called the secondary. If the secondary is a high-mass star (either a supergiant with spectral type earlier than B2, an Of star, an Oe star or a Be star), the binary is called a High-Mass X-ray Binary (HMXB). If the secondary is either a 'normal' main sequence star, a white dwarf, or a giant, the binary is called a Low-Mass X-ray Binary (LMXB). In most of the LMXBs, the primary (the NS or BH) is more massive than the secondary. Because the spectra of HMXBs are dominated by a strong emission spectrum of the secondary and are highly variable, HMXBs are not interesting for us to use as background sources. LMXBs have a more stable X-ray intensity and mostly continuum-dominated spectrum and are therefore more suitable for studying absorption of the ISM [10].

The primary and secondary usually orbit close to each other, which implies that they share a mutual gravitational equipotential line close to, or partially within the secondary. This means that the surface of the secondary may reach further out than the so-called Roche lobe, which is the region around a star in a binary in which matter is gravitationally bound to that star. It is not analytically determined, but can be approximated as [11]

$$r_{\mathrm{L}} = \frac{0.49q^{2/3}A}{0.6q^{2/3} + \ln(1 + q^{1/3})}, \tag{1.1}$$

where q is the mass ratio between the two stars ($q > 0$) and A is the orbital separation of the system. The outer edges of the secondary are thus usually not gravitationally bound to the secondary, and can therefore be accreted by the primary.

If the specific angular momentum L of the accreting matter is large enough for it to never hit the primary directly, the matter starts to rotate around the primary, creating an accretion disk. The orbital radius (assumed to be circular) of an accreted particle is determined by [12]

$$R = \frac{L^2}{GM_{\mathrm{s}}}, \tag{1.2}$$

where M_{s} is the mass of the secondary and G is the gravitational constant. However, as matter falls more inward, it loses gravitational potential energy. This energy is released as X-ray radiation, either heating up the accretion disk, or moving away from the binary to (after some time) reach us. If we assume the thin disk approximation (i.e. the disk lays in the orbital plane and has a small vertical scale compared to the horizontal scale), we can approximate the effective temperature distribution in the

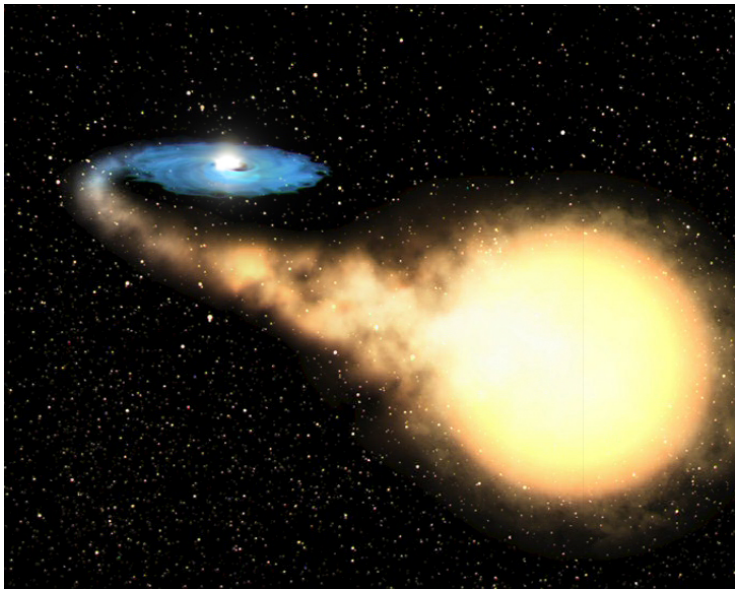

FIG. 1.1 – Artist's impression of an X-ray Binary.[1]

disk as [12]

$$T_{\text{eff}} = \left(\frac{3GM_{\text{s}}\dot{M}}{8\pi\sigma R^3}\right)^{1/4}\left[1-\beta\left(\frac{R_{\text{in}}}{R}\right)^{1/2}\right]^{1/4}, \tag{1.3}$$

where $\dot{M}$ is the accretion rate, σ is the Stefan-Boltzmann constant, R_{in} is the radius of the inner disc edge, β is a dimensionless number depending on the boundary conditions of R_{in}, and R is the radius. The radius R is determined by the initial angular momentum of the accreted matter as seen in Equation (1.2). For most of the disk, $R \gg R_{\text{in}}$, so that we can approximate Equation (1.3) further to

$$T_{\text{eff}} \approx \left(\frac{3GM_{\text{s}}\dot{M}}{8\pi\sigma R^3}\right)^{1/4} \propto R^{-3/4}. \tag{1.4}$$

Equation (1.4) tells us that the temperature will decrease when moving away from inner part of the accretion disk.

The primary is also surrounded by a so-called corona. The origin of the corona is still not clear, but it is believed to consist of moving hot electrons. Photons originating from the accretion disk (and also from the secondary) hit the electrons in the corona, resulting in inverse Compton scattering. The mean fractional energy gain of the photons per collision is [13]

$$\left\langle\frac{\Delta E_\gamma}{E_\gamma}\right\rangle = \frac{4k_{\text{B}}T_{\text{e}} - \langle E_\gamma\rangle}{m_{\text{e}}c^2}, \tag{1.5}$$

[1]Figure credits: ESA, NASA, and Felix Mirabel.

where k_{B} is the Boltzmann constant, T_{e} is the plasma temperature, $\langle E_\gamma \rangle$ is the average energy of the input photons, and $m_{\mathrm{e}}c^2$ is the electron rest energy. Notice that if $4k_{\mathrm{B}}T_{\mathrm{e}} > \langle E_\gamma \rangle$ in Equation (1.5), the scattering is called inverse Compton scattering because the net energy transfer is from electrons to photons. If $4k_{\mathrm{B}}T_{\mathrm{e}} < \langle E_\gamma \rangle$, it is the other way around (Compton scattering). In LMXBs, the scattering in the corona is inverse Compton scattering. The radiation energy of the comptonizing corona is therefore some higher than the radiation energy of the accretion disk.

The LMXB's flux thus originates from both the accretion disk and the Comptonizing corona. It is however not constant. Fluctuations arise from unstable accretion rates, causing a time-dependent flux. LMXBs are also known to have big dips in intensity, arising from the binary being in an almost equatorial LOS with respect to us. The dip in flux is probably caused by the obscuration along our LOS from the impact region between the accreted flow and the accretion disk [14]. Some of the radiation is then blocked off and a dip in the intensity of the source is measured.

Unfortunately, no X-ray binaries can be spatially resolved. In Figure 1.1 an artists impression of a LMXB is shown. It shows the way of creating an accretion disk around the primary by accreting matter from the secondary.

1.2 Collisional ionized equilibrium

The hot absorbing gas is believed to have temperatures around $\sim 10^6 - 10^7$ K [3,5–7,9]. When a gas reaches this high temperatures, it is believed to be in a Collisional Ionized Equilibrium (CIE) state. We can construct an equilibrium equation by looking at the total ionization ($z \to z+1$) and recombination ($z \to z-1$) rate coefficients ($\mathrm{cm}^3\,\mathrm{s}^{-1}$) of a certain ionization level z of ion $Z^{+\mathrm{z}}$, where the corresponding element is denoted by atomic number Z. The rate of change of the population density $N_{\mathrm{Z,z}}$ (cm^{-3}) of ion $Z^{+\mathrm{z}}$ reads [15]

$$\frac{1}{n_{\mathrm{e}}}\frac{\mathrm{d}N_{\mathrm{Z,z}}}{\mathrm{d}t} = N_{\mathrm{Z,z\text{-}1}}S_{\mathrm{Z,z\text{-}1}} - N_{\mathrm{Z,z}}(S_{\mathrm{Z,z}} + \alpha_{\mathrm{Z,z}}) + N_{\mathrm{Z,z+1}}\alpha_{\mathrm{Z,z+1}}, \tag{1.6}$$

where $S_{\mathrm{Z,z}}$ and $\alpha_{\mathrm{Z,z}}$ denote the total ionization and recombination rate coefficients respectively, and n_{e} is the electron number density (cm^{-3}). In Equation (1.6), diffusive terms which may represent dynamic effects have been neglected because these terms are negligible compared to the other terms for our case. However, if the CIE state is reached, the rate of change $\frac{\mathrm{d}N_{\mathrm{Z,z}}}{\mathrm{d}t}$ should become equal to zero. We can then simplify Equation (1.6) to an expression for the population density ratio

$$\frac{N_{\mathrm{Z,z+1}}}{N_{\mathrm{Z,z}}} = \frac{S_{\mathrm{Z,z}}}{\alpha_{\mathrm{Z,z+1}}} + \frac{\alpha_{\mathrm{Z,z}}}{\alpha_{\mathrm{Z,z+1}}} - \frac{N_{\mathrm{Z,z\text{-}1}}S_{\mathrm{Z,z\text{-}1}}}{N_{\mathrm{Z,z}}\alpha_{\mathrm{Z,z+1}}}. \tag{1.7}$$

The second term on the Right Hand Side (RHS) of Equation (1.7) can be neglected if we approximate that the $z+1 \to z$ recombination is much larger than the $z \to z-1$

recombination (i.e. $\alpha_{\mathrm{Z,z+1}} \gg \alpha_{\mathrm{Z,z}}$). Because this is true for the most abundant ions in the ISM at temperatures of $\sim 10^6 - 10^7$ K, this approximation can hold for our case. The third term on the RHS can also be neglected if we assume that the plasma is essentially a 2-state system (i.e. $N_{Z,z-1} \ll N_{Z,z}$). This assumption also holds for the most abundant ions in the ISM at temperatures of $\sim 10^6 - 10^7$ K. Equation (1.7) can thus be further approximated to

$$\frac{N_{\mathrm{Z,z+1}}}{N_{\mathrm{Z,z}}} = \frac{S_{\mathrm{Z,z}}}{\alpha_{\mathrm{Z,z+1}}}, \tag{1.8}$$

which tells us that the population density ratio of ionized particles is determined by the ratio of the ionization ($z \to z+1$) and recombination ($z+1 \to z$) rate coefficients. These rates themselves depend on the temperature, which will be further explained the Sections 1.2.1 and 1.2.2.

However, the CIE state assumption holds only if an optically thin plasma is assumed so that X-ray radiation does not dissipate away into interactions with other plasma particles, and if there are no external effects that alter the ionization balance (e.g. photo-ionization can be neglected). It is also assumed that the plasma density is sufficiently low so that on average all ions are in the ground state and excited atoms decay by spontaneous radiation, and that the plasma particles follow a Maxwellian distribution of velocities.

1.2.1 Ionization rate coefficient

Collisional ionization occurs when an electron collides with an (ionized) particle. It can happen either via Direct Ionization (DI) or via Excitation-Autoionization (EA) [15],

$$Z^{+\mathrm{z}} + e^- \to Z^{+(\mathrm{z+1})} + 2e^-, \qquad \text{(DI)} \tag{1.9a}$$

$$Z^{+\mathrm{z}} + e^- \to (Z^{+\mathrm{z}})^* + e^- \to Z^{+(\mathrm{z+1})} + 2e^-. \qquad \text{(EA)} \tag{1.9b}$$

DI occurs when an electron collides with an ion, removing an electron from the ion. In the EA case, the plasma particle is first ionized to an ionization level above the ionization energy (first arrow in Equation (1.9b)) after which autoionization follows (second arrow in Equation (1.9b)). Ionization by ion-impact has been neglected.

The total rate coefficient $S_{\mathrm{Z,z}}$ can be written as a superposition of the DI and EA rate coefficients,

$$S_{\mathrm{Z,z}} = S^{\mathrm{d}}_{\mathrm{Z,z}} + S^{\mathrm{a}}_{\mathrm{Z,z}}. \tag{1.10}$$

The two rate coefficients on the RHS depend (among other things such as particle velocities and energies) on the temperature. The DI rate coefficient scales with the temperature as $S^{\mathrm{d}}_{\mathrm{Z,z}} \propto T^{1/2}\chi^{-1}\exp(-\chi/k_{\mathrm{B}}T)$, where χ is the ionization

energy. In the case of the EA, it gets some more complicated because the inner quantum energy levels start to play a role. However, if the excitation energy of the autoionizing level E_0 is large ($E_0/k_\mathrm{B}T \gg 1$), the EA rate coefficient scales as $S^\mathrm{a}_\mathrm{Z,z} \propto T^{-1/2}E_0^{-1}\exp(-E_0/k_\mathrm{B}T)$.

1.2.2 Recombination rate coefficient

Recombination can happen via various mechanisms. For a CIE state plasma two of these processes are the most dominant, radiative recombination (RR) and di-electronic recombination (DR). Because the temperature in the hot plasma is high, charge transfer does not have to be taken into account. Also 3-body recombination is neglected because we assume a low density plasma. The processes of RR and DR are shown in Equations (1.11a) and (1.11b) respectively [15],

$$Z^{+(\mathrm{z}+1)} + e^- \rightarrow Z^{+\mathrm{z}} + h\nu, \qquad \text{(RR)} \qquad (1.11a)$$

$$Z^{+(\mathrm{z}+1)} + e^- \rightarrow (Z^{+\mathrm{z}})^{**} \rightarrow Z^{+\mathrm{z}} + h\nu + h\nu' + h\nu'' + ... \qquad \text{(DR)} \qquad (1.11b)$$

In the case of RR, an ionized particle absorbs an electron, producing a photon (with energy $h\nu$). In the case of DR, the electron is first absorbed, after which it radiates down in multiple transitions, producing multiple photons (with different energies $h\nu$, $h\nu'$, $h\nu''$, ...) depending on the number of transitions. If the ion would autoionize again directly after the electron absorption, no recombination would take place and the system would remain unaltered.

Similarly to the the total ionization rate coefficient (Equation (1.10)), the total recombination rate coefficient can be written down as a superposition of the two recombination rate coefficients,

$$\alpha_\mathrm{Z,z+1} = \alpha^\mathrm{r}_\mathrm{Z,z+1} + \alpha^\mathrm{d}_\mathrm{Z,z+1}. \qquad (1.12)$$

The two rates on the RHS also have a temperature dependence similar to the ionization rate coefficients. The RR rate coefficient scales via $\alpha^\mathrm{r}_\mathrm{Z,z+1} \propto 10^{-11} z_\mathrm{e}^2 T^{-1/2}$, where z_e is the effective nuclear charge defined by $\chi_{m_0} = E_H z_e^2/m_0^2$, where χ_{m_0} is the ionization energy of the recombined ion in the ground state with principal quantum number m_0 and E_H is the ionization energy of hydrogen. The DR rate coefficient scales via $\alpha^\mathrm{d}_\mathrm{Z,z+1} \propto 10^{-16} T^{-3/2} \sum_s B_s \exp(-E_s/k_\mathrm{B}T)$, where E_s is energy difference between autoionizing state s and the ground state, and B_s is a coefficient depending on atomic rates.

The CIE state is thus reached when the ionization rate, produced by DI and EA, is balanced by the recombination rate by means of RR and DR. However, the approximated Equation (1.8) was introduced to give analytical solutions. In numerical simulations we can use the full equilibrium equation given by Equation (1.7).[2]

[2]For more information regarding CIE state plasmas and rate coefficients, we would refer you to [15].

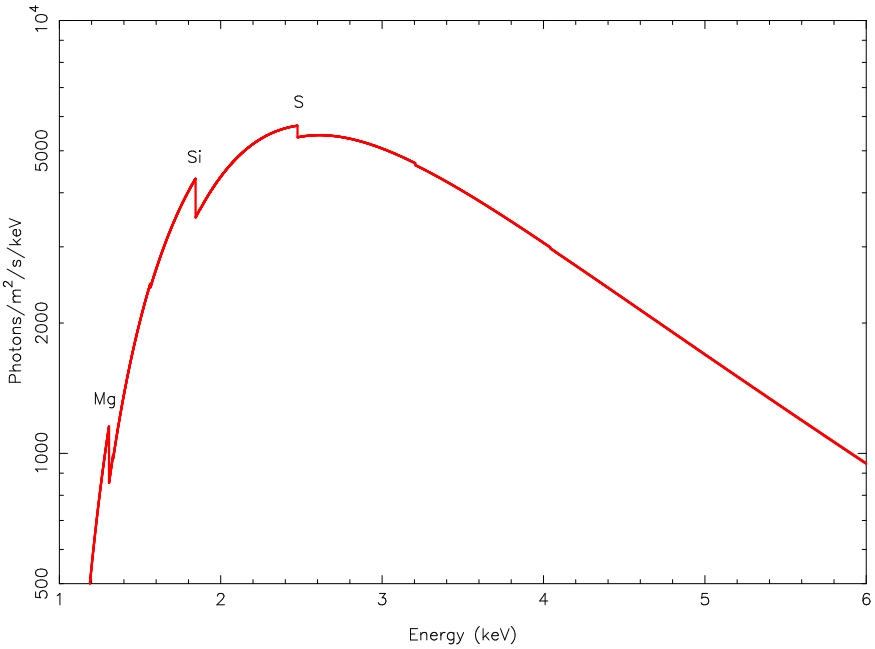

FIG. 1.2 – A schematic model of a featureless spectrum (i.e. no absorption lines). Absorption by the cold ISM ($N_H = 4 \times 10^{22}\,\mathrm{cm}^{-2}$) is nevertheless present, which can be seen in the absorption edges and the curvature at lower energy.

1.3 Absorption Spectra

A background LMXB creates a continuum spectrum. At small energies ($E \lesssim 3\,\mathrm{keV}$) the spectrum is dominated by the radiation from the accretion disk, which has the form of a black body function. At larger energies ($E \gtrsim 3\,\mathrm{keV}$), the spectrum starts to be more and more dominated by the comptonizing corona of the LMXB, giving the spectrum its power-law shape tail. If no absorption would take place, the spectrum would be featureless. However, because the spectrum is always absorbed by the cold ISM, absorption is never absent. In the soft X-ray band, absorption by the cold ISM is seen as a curvature over the lower energy band ($\lesssim 3\,\mathrm{keV}$), with absorption edges being produced by photoelectric absorption of neutral atoms. The latter can be seen in a spectrum as sharp dips in intensity. To get an understanding on how much radiation is absorbed by intervening gas, one needs the (number) density of the absorber. The density, however, is very hard to obtain, while the so-called column density can easily be measured. The column density is calculated by an integral over the number density of a section of the unit cylinder along the LOS,

$$N = \int n(z)\,\mathrm{d}z, \tag{1.13}$$

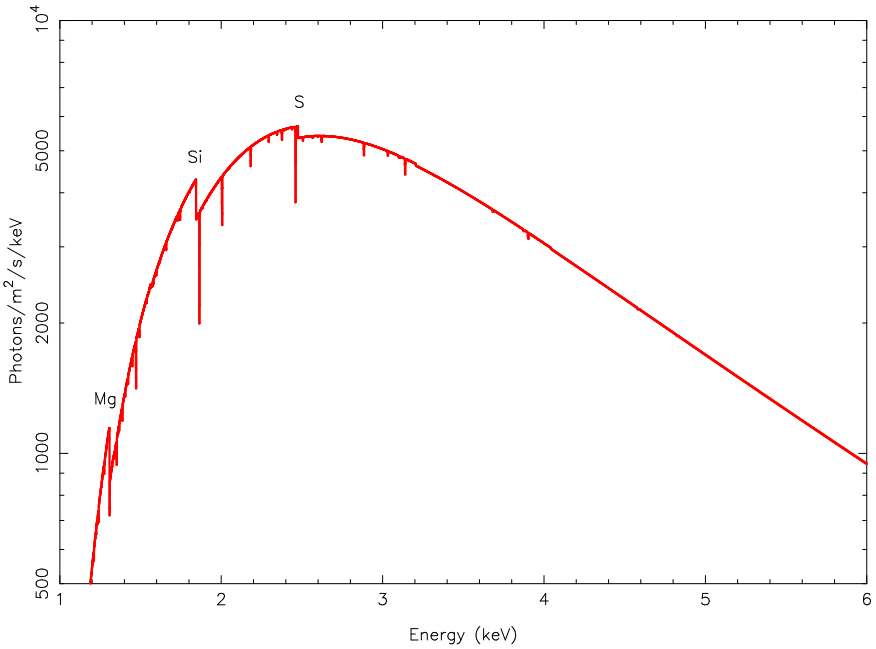

FIG. 1.3 – Same spectrum as in Figure 1.2, however now a hot absorber has been added with a column density $N_{\rm H} = 10^{21}\,{\rm cm}^{-2}$ and a temperature $k_{\rm B}T = 1\,{\rm keV}$. Note the absorption lines appearing because of the hot absorber.

and is often measured in cm^{-2}. A schematic figure of a spectrum absorbed by only the cold ISM with a hydrogen column density N_H of $4 \times 10^{22}\,\mathrm{cm}^{-2}$ is shown in Figure 1.2. Note that absorption edges are present at e.g. 1.3 keV (Mg), 1.8 keV (Si) and 2.5 keV (S).

However, if intervening hot gas in CIE state is present along our LOS, absorption lines will be imprinted on the spectrum, depending on the density and temperature of the hot gas. This creates an absorption spectrum as shown in Figure 1.3. Each absorption line represents absorption of a certain ion, which we can identify by looking at the energy of the absorption line. By looking at the depth of the absorption line, one can estimate the column density of that ion. By looking at the line ratios, one can calculate the temperature of the gas. Therefore, we can obtain the temperature and the column density of the hot gas by fitting it with a CIE absorption model.

2 Data analysis

In this section we illustrate the data analysis. First we discuss the choice of our samples in Section 2.1, after which the conversion of raw the data to a suitable form will be discussed in Section 2.2. The method of analyzing the data is explained in Section 2.3.

2.1 Sample selection

As already mentioned in Section 1.1, only LMXBs are used here as background sources. For this study, 12 LMXBs have been examined, which have been selected to have low galactic latitude ($|b| \lesssim 1.5°$) to guarantee that the sources lied in the Galactic plane. The sources were also selected to have a high count rate to ensure a high signal-to-noise ratio, and a good possibility of showing absorption lines because of the high column density towards the source. The used sources are listed in Table 1.

TABLE 1
Used Sources

Source	Alternative Name	(l, b) (deg)	D^a (kpc)		OBSID	$T^{\rm obs}$ (s)
4U 1323-62	–	(307.03, +0.46)	10	[16]	3826	38009
4U 1608-52	V* QX Nor	(330.92, -0.85)	5.8	[17]	12127	23078
4U 1624-49	BIG DIPPER	(334.92, -0.26)	15	[18]	4559	73365
4U 1630-47	X Nor X-1	(336.91, +0.25)	10	[19]	4568	49986
4U 1728-34	SLOW BURSTER	(354.30, -0.15)	5.2	[20]	6568	49297
IGR J17497-2821	–	(0.95, -0.45)	8	[21]	6613	19701
4U 1811-17	V* V5512 Sgr / GX 13+1	(13.52, +0.11)	7	[22]	11818	23026
4U 1642-45	GX 340+00	(339.59, -0.08)	11	[23]	6631	25034
4U 1702-429	X Ara X-1	(343.89, -1.32)	5.5	[24]	11045	49143
1E 1740.7-2942	GREAT ANNIHILATOR	(359.12, -0.11)	8.5	[25]	2491	61159
SAX J1747.0-2853	[KRL2007b] 275	(0.21,- 0.24)	7.5	[26]	1935	28590
GX 5-1	–	(5.08, -1.02)	8.5	[27][b]	10692	8147.1

NOTE.– l and b represent the Galactic longitude and latitude respectively, D the distance to the source, OBSID the observation ID, and $T^{\rm obs}$ the exposure time.
[a] Distances as assumed/calculated in the references.
[b] In [27], an upper limit of 9 kpc has been determined. For our study we used 8.5 kpc. This is within the error of the fluxes, so has no consequences for the results.

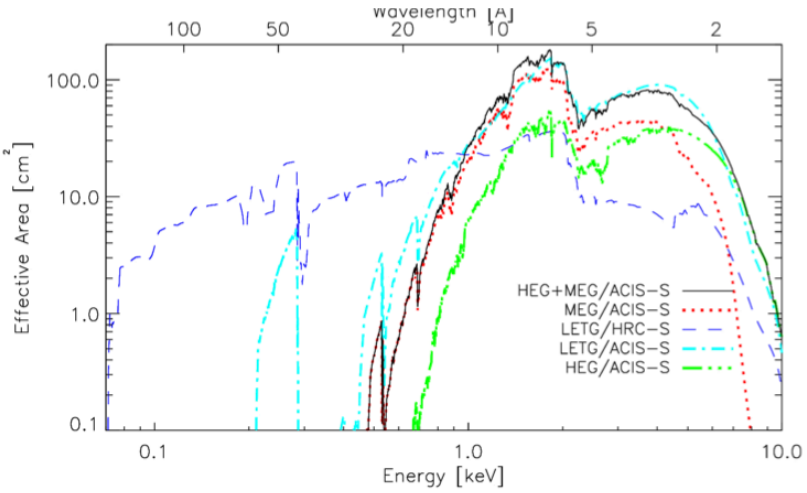

FIG. 2.1 – The effective areas of the different *Chandra* gratings.[3]

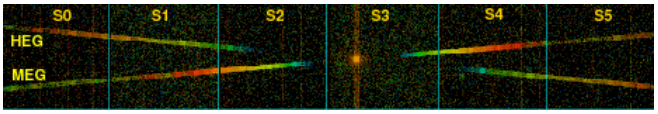

FIG. 2.2 – Detected spectrum on the ACIS. The colors indicate the energies of the photons (red for higher energies, blue for lower energies).[3]

2.2 Data conversion

We use the High Energy Transmission Grating (HETG) [28] from the *Chandra*-satellite. This is coupled with by the Advanced CCD Imaging Spectrometer (ACIS), which can make X-ray images and measure the energies of the incoming X-ray radiation. The HETG is divided into two different gratings, the High Energy Grating (HEG) and Medium Energy Grating (MEG). The HETG covers an energy range of about 0.4-10 keV, in which the HEG as the highest effective area for higher energies and the MEG for lower energies. The effective area of the HEG and MEG are shown in Figure 2.1, in which the green and red dotted lines represent the effective areas of the HEG and MEG respectively. The black solid line represents the effective area of the HETG altogether.

The HETG diffracts the incoming X-rays in two different directions depending on the grating (HEG or MEG), forming a X shape as shown in Figure 2.2. The two lines on the right represent the positive diffraction orders, the two lines on the left the negative orders, where the zeroth-order is seen as the dot in sector S3. For our study, we use the 1st diffraction orders which benefit of a higher effective area.[4].

[3]Figure credits: http://cxc.harvard.edu/proposer/POG/html/chap8.html

[4]For more instrumental information, we would refer you to the Proposers' Observatory Guide: http://cxc.harvard.edu/proposer/POG/html/index.html

The data was downloaded from the TGcat database[5]. Observations for each source were chosen depending on their exposure time and overall quality (e.g. no anomalous behaviour in the spectrum which could indicate instrumental failure). In most cases a longer exposure time implied a better spectrum because more photons could be measured. A very bright source, however, introduces pile-up, which means that the count rate of incoming photons is higher than the read-out time of the CCDs. Based on this, we chose one observation for each source. The used observations, indicated by the observation ID (OBSID) and corresponding exposure time $T^{\rm obs}$, are listed in Table 1.

The data was reprocessed using the CIAO software (version 4.7). This software combines the first order spectra of both the HEG and MEG into one spectrum for each. To analyze the data with our spectral fitting program SPEX, the data had to be converted into a suitable format, which was realized using the Trafo tool (version 1.03).

2.3 Analysis

The data was analyzed using SPEX version 2.05.04[6]. At higher energies ($\gtrsim 8\,\mathrm{keV}$), the effective area of the HETG gets too low to detect a sufficient source flux. At lower energies ($\lesssim 1\,\mathrm{keV}$), the count rate would be so low that no sufficient source flux would be observed. Therefore, the range of the HEG was set to $\sim 1.2 - 8\,\mathrm{keV}$ and the range of MEG to $\sim 1 - 5\,\mathrm{keV}$. The range differed per source because the count rates of the sources varied, and because for some observations either HEG or MEG would not function properly at certain energies. The spectrum of each source was rebinned by a factor 5 to a bin size of $62.5\,\mathrm{bins/mÅ}$. To avoid complications due to the the absorbing dust in the ISM, the absorption edges of neutral Si (1.84 keV) and neutral Mg (1.31 keV) were removed from the spectrum since these elements are abundant in dust.

The continuum was fitted with a disk black body (dbb) model and a Comptonization (comp) model representing the accretion disk and comptonizing corona respectively. However, if the parameters of the dbb model were unconstrained, the dbb model was replaced with a simpler black body (bb) model. The bb model approximates the accretion disk as a black body radiator with a single temperature, and therefore is less complicated and easier to fit. Similarly, if the parameters of the comp model were unconstrained, a power-law (pow) model would be introduced. The pow model approximates the spectrum of the comptonizing corona as a power-law, which is a fairly good approximation as one can note in Figure 1.2.

[5]Link: http://tgcat.mit.edu/

[6]For more information regarding the specifications we would refer you to the SPEX manual: https://www.sron.nl/files/HEA/SPEX/manuals/manual.pdf

TABLE 2
Used models

Model	Abbreviation	Free parameters
Disk black body	dbb	K_1, $k_\mathrm{B}T$
Black body	bb	K_1, $k_\mathrm{B}T$
Comptonization	comp	K_2, $k_\mathrm{B}T_0$, $k_\mathrm{B}T_1$, τ
Power-law	pow	K_2, Γ
CIE absorption	hot	N_H, $k_\mathrm{B}T$, zv
Photo ionized absorption	xabs	N_H, $\log[\xi]$, zv
Gaussian	gaus	K_3, E, $FWHM$

NOTE.– K_1 is the normalization of the (disk) black body (m^2), K_2 the normalization of the Comptonization and power-law ($\mathrm{ph\,s^{-1}\,keV^{-1}}$), K_2 the normalization of the Gaussian ($\mathrm{ph\,s^{-1}}$), T the temperature (K), T_0 the average temperature of the seed photons (K), T_1 the plasma temperature (K), τ the optical depth, Γ the photon index, N_H the column density ($\mathrm{cm^{-2}}$), zv the average velocity ($\mathrm{km\,s^{-1}}$), $\log[\xi]$ the ionization parameter, E the line energy (keV), and $FWHM$ the Full Width Half Maximum (keV).

The X-ray radiation will be absorbed by the hot and cold phase of the ISM. For the absorption of these two phases, two CIE absorption (hot) models were used. We assume the cold ISM to be in a neutral phase. Therefore the temperature ($k_\mathrm{B}T$) was frozen to $5 \times 10^{-4}\,\mathrm{keV}$ and the column density was the only free parameter. For the hot gas, besides the column density, also the temperature and the average velocity were free parameters. The average velocity was freed to verify that the absorption was caused by non-outflowing hot gas. If the average velocity would have a constrained negative high value, the absorption would be by outflowing gas which is intrinsic to the source. If this was the case, a photo-ionized absorption (xabs) model was used to represent the outflowing gas. In the xabs model the (logarithm of the) ionization parameter is defined as

$$\xi = \frac{L}{nR^2},$$

where L is the ionizing luminosity, n the number density of the gas, and R the distance of the gas to the source. It therefore represents absorption by gas nearby the source. The average velocity was freed to represent the outflow. The xabs model was also used for characterising gas of the dipping sources because dips arise from an eclipsing binary and from photo-ionized absorption by the accretion disk [29].

However, if no hot gas was observed, the parameters of the hot model were unconstrained or converging to 0. For these sources, the temperature was fixed at three different values corresponding with absorption lines of abundant ions: 1.0 keV ($\mathrm{Ne_X}$), 1.4 keV ($\mathrm{Mg_{XI}}$), and 1.9 keV ($\mathrm{Si_{XI}}$). For each of these three temperatures, the spectrum was fitted and an (upper limit for the) column density was measured which the hot gas should have if it had the corresponding temperature. The average velocity was fixed to 0 to assure non-outflowing gas.

In some spectra an Fe Kα emission line showed up at 6.4 keV. This emission line was fitted using a Gaussian (gaus) model. The gaus model was also used to fit the instrumental enhancement for high-flux sources at $\sim$ 2.05 keV [30], and for other Gaussian-like features in the spectrum. An overview of the used models and their free parameters is shown in Table 2.

The spectra were fitted using Poisson statistics (from now on called C-statistics) [31]. The HEG and MEG spectrum were jointly fit, using one set of parameters. During the fitting process, the goal was to attain a C-stat/d.o.f. (degrees of freedom) of ~ 1. If the lowest C-stat/d.o.f. was reached, it was checked whether the parameters would have physical values and where they were constrained within their parameter range, after which the errors of all the parameters were calculated and reported.

3 Results

In this section the results are reported. In Appendix A, the tables with data as outputted by SPEX are listed. In the spectra of 4U 1323-62, 4U 1608-52, 4U 1728-34, IGR J17497-2821, 4U 1811-17, 4U 1642-45 and GX 5-1 (tables A1 and A2), a hot absorber was observed. In the spectra 4U 1624-49, 4U 1630-47, 4U 1702-429, 1E 1740.7-2942 and SAX J1747.0-2853 (tables A3-A7) no hot absorber was observed and an upper limit for the column density was measured for each of the three temperatures mentioned in Section 2.3. In the second and third columns of Table 3, we reported per source whether a hot model or (multiple) xabs model(s) were used to fit the spectra.

TABLE 3
Best-fit results

Source	# hot	# xabs	N_H^{hot} ($10^{20}\,\mathrm{cm}^{-2}$)	T^{hot}) ($10^6\,\mathrm{K}$)
4U 1323-62	1	1	100^{+40}_{-30}	13 ± 2
4U 1608-52	1	1	$0.8^{+1.8}_{-0.3}$	$8.4^{+3.4}_{-1.4}$
4U 1624-49	0	2	–	–
4U 1630-47	0	1	–	–
4U 1728-34	1	0	$3.2^{+1.3}_{-1.2}$	12 ± 2
IGR J17497-2821	1	0	20^{+11}_{-9}	11^{+3}_{-2}
4U 1811-17	1	1	$0.93^{+0.40}_{-0.62}$	$4.5^{+5.8}_{-2.3}$
4U 1642-45	(1)	1	< 3.0	13^{+5}_{-3}
4U 1702-429	0	1	–	–
1E 1740.7-2942	0	0	–	–
SAX J1747.0-2853	0	1	–	–
GX 5-1	(1)	1	$4.3^{+1.0}_{-1.3}$	$8.8^{+1.2}_{-1.7}$

NOTE.– The best-fit results of each source. Indicated is whether a hot absorber was observer and whether an photo ionized absorber was detected. If a hot absorber was found, the column density and temperature are also reported. The temperature is calculated by dividing the temperatures in Tables A1 and A2 by the Boltzmann constant. Note that for the sources 4U 1642-45 and GX 5-1, it is questioning whether there is an actual hot absorber (4U 1642-45), or whether the hot absorber is related to the GC (GX 5-1).

For the sources showing a probable hot absorber, the column density and temperature are stated in the fourth and fifth column in Table 3. One can note that in case of the sources 4U 1642-45 and GX 5-1, the number of hot models is between brackets. This is indicated because for these two sources we are not sure whether the hot absorption is due to hot gas near the GC. For 4U 1642-45, the column density is an upper limit where the temperature is constrained, which could imply that no hot absorber is present along its LOS. In the case of GX 5-1, a constrained outflow velocity is measured ($-200^{+80}_{-100}\mathrm{km\,s}^{-1}$), which could indicate that the measured absorption is

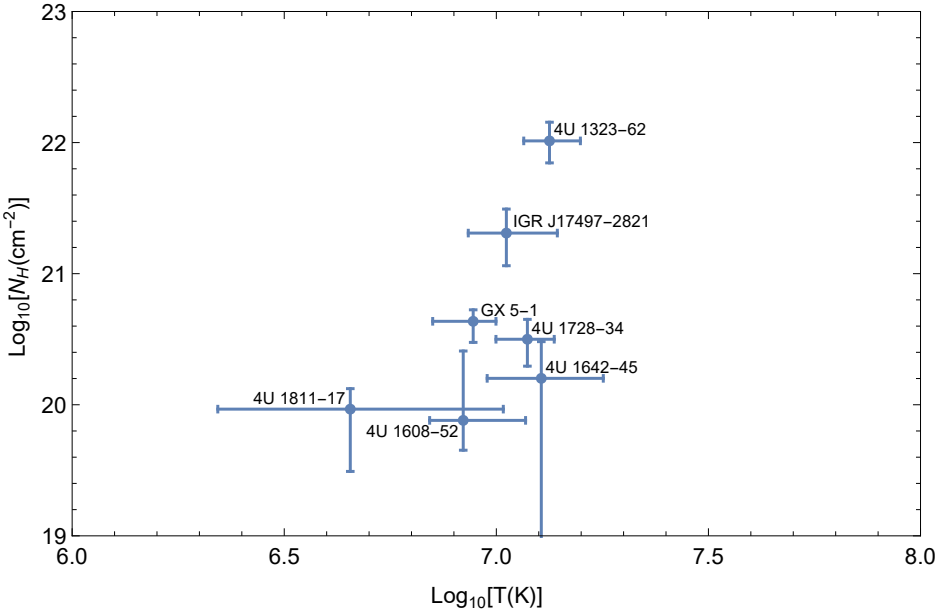

FIG. 3.1 – The measured data points for the sources which showed a hot absorber, plotted in a log-log plot of the column density against the temperature.

not produced by the hot ISM near the GC. The data points are plotted in a column density-temperature graph in Figure 3.1. The sources 4U 1642-45 and GX 5-1 are also added to the figure. Note that the discrepancy in column densities is a lot higher than the discrepancy in temperature (factor 100 against a factor 3).

For the sources which did not show a hot absorber in their spectrum, the upper limits for the column densities measured at the three different temperatures are stated in Table 4. Note that for all the sources the upper limits increase with increasing temperature.

TABLE 4
Best-fit results non-absorbed sources

	Temperature		
Sources	12×10^6 K	16×10^6 K	22×10^6 K
4U 1624-49	< 6.3	< 12	< 22
4U 1630-47	< 22	< 55	< 81
4U 1702-429	< 1.2	< 1.2	< 1.4
1E 1747.0-2942	< 16	< 22	< 35
SAX J1747.0-2853	< 1.4	< 1.8	< 3.0

NOTE.– The upper limits for the column densities for the sources which did not show a hot absorber, measured at three different temperatures. The column densities are expressed in 10^{20} cm^{-2}.

4 Discussion

Of the 12 sources we fitted, 5 sources show no hot absorber along their LOS, and 2 sources show a questionable hot absorber. This could be correlated to the direction of the source. Furthermore, some sources seem to be closer to us than the GC itself, indicating that a possible hot absorber along their LOS is not situated near the GC. However, the absorption could also be a feature of the local bubble or a supernova remnant. These cases will be discussed in this section. We also discuss the parameters of the xabs model in our fits.

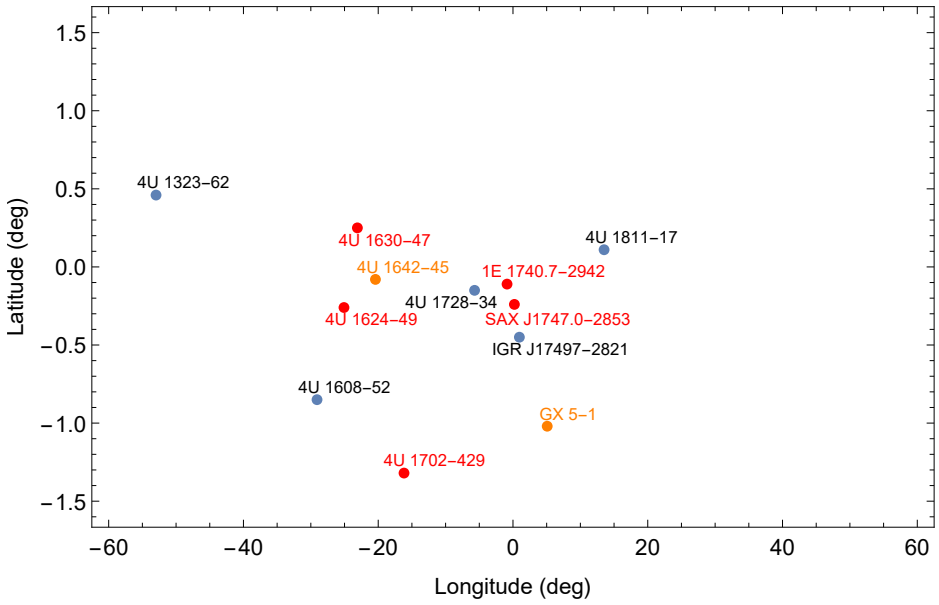

FIG. 4.1 – A graph showing the location of the background sources. Note that the sources which showed a hot absorber along their LOS are shown as blue dots, the sources with a questioning hot absorber as orange dots, and the sources without hot absorber as red dots.

In Figure 4.1, we plot the locations of the sources as function of their Galactic coordinates. The sources which show a hot absorber along their LOS are shown as blue dots, the sources with a questioning hot absorber as orange dots, and the sources which show no hot absorber as red dots. From a first look, no direct correlation between a hot absorber and the direction of the LOS is visible. We thus have to search for other reasons.

It was already known that the spectra of 1E 1740.7-2942 and SAX J1747.0-2853 were heavily absorbed by the cold ISM [25, 26]. This can also be seen in our results as high column densities. A hot absorber could also lay along the LOS to these sources, but because of the high absorption by the cold ISM, it could not be measured.

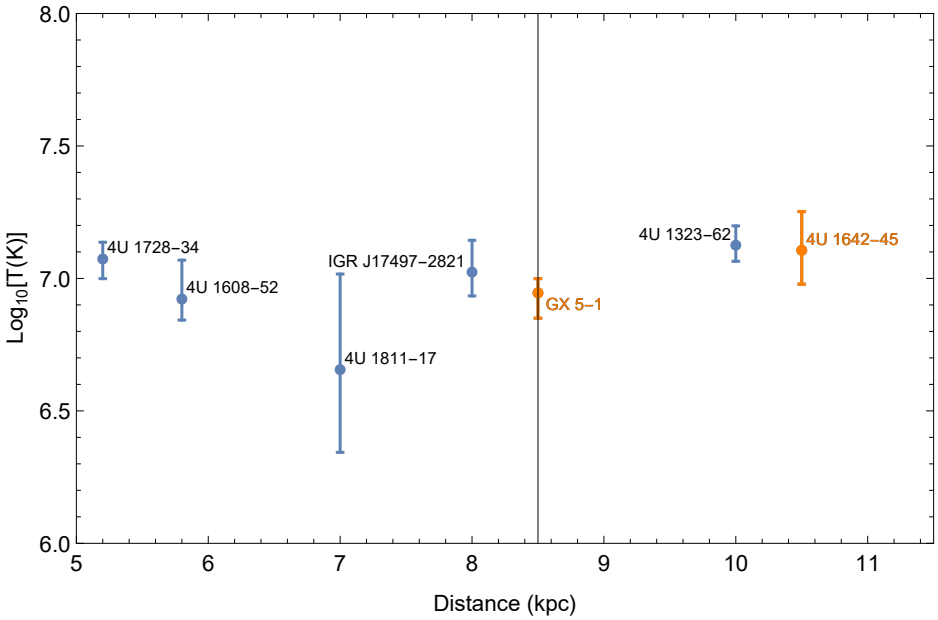

FIG. 4.2 – The measured temperatures of the hot absorbers plotted against the distance to the background sources. The questionable hot absorbers are again represented as orange dots. The distance to the GC is indicated by the black vertical line.

The sources 4U 1323-62 and 4U 1624-49 are known dippers [29]. This implied that the spectra had a relatively low count rate, hence that a possible hot absorber was difficult to measure. In the case of 4U 1624-49, the opacity of the gas was remarkably high, resulting in very low count rates (ergo the name of the source: BIG DIPPER). A possible hot absorber could thus be along its LOS but could not measured because of the low count rates. In the case of 4U 1323-62, despite the low count rate, a hot absorber was measured.

In the spectra of 4U 1630-47 and 4U 1702-429, no peculiar features were visible. One note can be that the spectrum of 4U 1630-47 could not be fitted properly (C-stat/d.o.f=1203/515), and therefore no hot absorber could be found. However, there may also just be no hot absorber along its LOS. A note for 4U 1702-429 could be that it has a higher galactic latitude and therefore does not lay in the vicinity of the GC, hence that no hot absorber may lay along its LOS.

One could also search for a correlation between the column density of hot absorbers as a function of the LOS. A very high column density was observed for 4U 1323-62 (order of magnitude higher than the next highest column density), which is farthest-out laying source in Figure 4.1. The hot absorber measured along this LOS lays far out from the GC, and may therefore not be related to the GC activity.

Next we discuss the distances towards the sources. Unfortunately, the distance to the GC itself is not exactly known, but assumed to be between 7 kpc and 9 kpc [32].

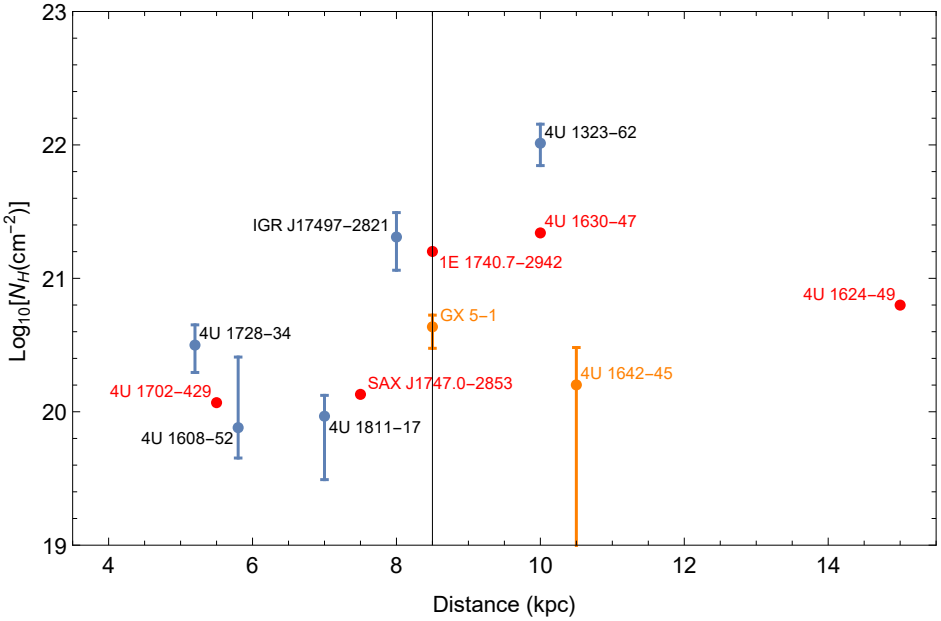

FIG. 4.3 – The measured column densities of the hot absorbers plotted against the distance to the background sources. The questionable hot absorbers are again represented as orange dots, and the red dots represent the upper limits at $T = 12 \times 10^6$ K for the sources without a hot absorber along their LOS. The distance to the GC is indicated by the black vertical line.

We assume a distance of 8.5 kpc. A figure of the temperature of the hot absorber plotted against the distance to background source is shown in Figure 4.2. In this figure the distance to the GC is shown as the vertical black line at 8.5 kpc. Note that the sources 4U 1728-34, 4U 1608-52 and 4U 1811-17 have smaller distances than the GC itself, hence the hot absorbers in the spectra of these sources may be in the Galactic plane but possibly not connected with the GC.

We can also take a look at the correlation between the column density of the hot absorber and the distance to the background source. A plot of this is seen in Figure 4.3. It would seem from the figure that the average column density of the hot absorber makes a jump at $D \sim 8$ kpc , especially if we also add the upper limits for the column densities at $T = 12 \times 10^6$ K (the lowest of the three temperatures) of the sources without hot absorber. The jump (of about a factor 10) is an indication that a hot absorber may be present near the GC.

However, the absorption could have taken place anywhere between the background source and us. It could therefore also be a feature of a Local Bubble (LB). This is nevertheless not the case because the temperature of the gas in the LB does not exceed temperatures of about $\lesssim 10^6$ K [33]. This is about an order of magnitude lower than temperatures we measure, hence absorption by the LB can be excluded.

The absorption may also be a feature of a supernova remnant (SNR). The interior of a SNR can contain gas with temperatures of $\gtrsim 10^{6.5}\,\mathrm{K}$ [34], which can easily get as high as $\sim 10^7\,\mathrm{K}$. This could especially be an explanation for the absorption towards the sources 4U 1323-62, 4U 1608-52, 4U 1728-34 and 4U 1811-17. As already discussed, the source 4U 1323-62 lays too far out of the GC, and the distance to 4U 1608-52,4U 1728-34 and 4U 1811-17 is lower than the GC. The hot absorbers along the LOS of these sources can therefore not be of GC origin, yet still they show hot absorbers with temperatures of $\sim 10^7\,\mathrm{K}$. One would not expect the hot ISM to have these temperatures far outside the GC. This absorption may thus be due to SNRs. A SNR could also explain the absorption towards GX 5-1, as hot gas in SNRs tends to have high velocities.

Still, we believe that the hot absorber in the spectrum of IGR J17497-2821 is in fact of GC origin. Although the source IGR J17497-2821 is situated somewhat closer to us than the GC as shown in Figure 4.2, we nevertheless still believe that the hot absorber in the spectrum of IGR J17497-2821 may be of GC origin since the source still lies relatively close to the GC.

4.1 Gas intrinsic to the source

Other than the hot gas, it may be interesting to look at the fit parameters of the xabs model. We plot the measured column density of the xabs model against the corresponding ionization parameter in Figure 4.4. For the sources that showed no hot absorber, we choose the xabs values corresponding to the fit with $T^{hot} = 12 \times 10^6\,\mathrm{K}$. It is immediately notable that the data points can divided into two regions , indicated in Figure 4.4 as the red regions. Although the photo ionized absorber in the spectrum of SAX J1747.0-2853 has error margins reaching out to typical values for region 1, we assume it to be part of region 2.

Region 1 consists of data points with lower ionization parameter ($\log[\xi] \sim 2.55 \pm 0.55$), and region 2 of data points with higher ionization parameter ($\log[\xi] \sim 4.80 \pm 0.95$). The parameter ξ depends on many factors. A higher ξ could imply a higher ionization luminosity as $\xi \propto L$. At the same time $\xi \propto \frac{1}{nR^2}$, hence the closer the gas and the lower the density, the higher ξ. We expect no values higher than 6 because the absorber would then be extremely highly ionized, and no values lower than 2 since these would be difficult to detect because of the high neutral column densities along the LOS. This erases the features of gas with $\log(\xi) < 2$. Nevertheless, no gas with $\log[\xi] \sim 3-4$ is observed, This gas may still be there, but with a low column density.

The column densities of the sources in region 2 ($\log[N_H^{xabs}] \sim 23.5 \pm 1.0$) are about 2 orders of magnitude higher than the column densities of region 1 ($\log[N_H^{xabs}] \sim 21.0 \pm 1.5$). It is, however, already known that a correlation between the column density and the ionization parameter exist [35].

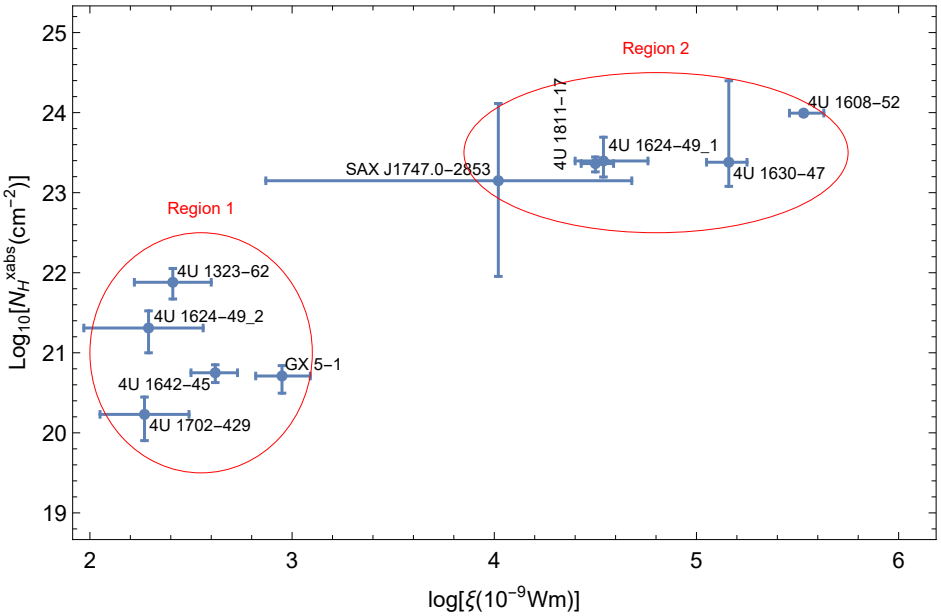

FIG. 4.4 – The column densities of the photo ionized absorbers plotted against their corresponding ionization parameters as measured with the xabs model. Two regions in which all data points are located are indicated in red. Although the photo ionized absorber in SAX J1747.0-2853 has error margins reaching out to typical values for region 1, we assume it to be part of region 2.

5 Conclusion

There is an indication of existing hot gas with a temperature of $\sim 10^7\,\mathrm{K}$ in and near the GC. The hot gas has column densities varying between $\sim 10^{21} - 10^{22}\,\mathrm{cm}^{-2}$. These results agree with earlier research [9]. However, because of the few observations, no further constrained temperature and column densities can be achieved.

It is also observed that intrinsic absorption of X-ray binaries has a correlation between the column density of the absorber and the corresponding ionization parameter. This also agrees with earlier research [35].

The results were tested by looking for possible explanations for the absorption. We observed a hot absorber along the LOS of 7 sources. Two of the hot absorbers were not assumed to be of GC origin because they had a constrained outflow velocity (GX 5-1), or a upper limit for the column density (4U 1642-45). Four of the observed hot absorbers lay along the LOS of sources which did not lay behind the GC (4U 1608-52, 4U 1728-34 and 4U 1811-17 were too close, 4U 1323-62 was too far out), and therefore may not be of Galactic central origin. Still we believe that the hot absorber along the LOS of IGR J17497-2821 is in fact of GC origin. It was concluded that the absorption was not a feature of the LB because the LB temperatures do not attain the measured temperatures. However, the absorption could have been a feature of intervening SNRs, as the gas temperature may be consistent with that of hot gas in SNRs. This could especially be an explanation for the absorption towards sources that did no lie behind the GC, and for GX 5-1 since hot gas in SNRs can have high velocities.

Future research can be done by looking at more sources in the vicinity of the GC. A constrained temperature dependence can then be obtained. Future missions will have an increased energy resolution of $E > 2\,\mathrm{keV}$, which will allow us to detect multiple ions of the hot phase and do more sophisticated studies, e.g. element abundances in the ISM. One can search for a possible time variability of the spectra to see if the absorber varies in time (if it belongs to the ISM, it is not expected to vary). For this, one can use phase resolved spectroscopy to see if the gas parameters vary as a function of the orbit, and check for long term changes of the gas (e.g. reflecting flux variations). For the dipper sources one can use time resolved spectroscopy to attain the dipper's parameters such as frequency and the luminosities of both the dip-stage and the active-stage. Emission of the hot gas observed in an empty field nearby the source may determine whether it is located within a SNR (e.g. absorption is only in front of a background source, emission is everywhere).

6 Acknowledgements

Doing my bachelors research at the SRON was very pleasant. I would therefore like to thank Dr. Elisa Costantini for giving me this enjoyable place to do my research, and for supervising my research. Without your knowledge, it would have been a very difficult task. I would also like to thank Dr. Tomislav Prokopec, for willing to be my supervisor at the University. Without you, doing my research at the SRON would not have been possible. My thanks also go to Sascha Zeegers and Laura di Gesu for helping me with learning the basics of SPEX, and of course the rest of the Astrophysics group for the many enjoyable coffee breaks. You made my time at SRON memorable.

Appendix A Data Tables

TABLE A1
Best-fit data for 4U 1323-62, 4U 1608-52, 4U 1728-34 & IGR J17497-2821

	4U 1323-62	4U 1608-52	4U 1728-34	IGR J17497-2821
Distance (kpc)	10	5.8	5.2	8
$K^{bb}(10^{16}\,\mathrm{m}^2)$	$(2.3^{+0.5}_{-0.4})\times10^{-8}$	–	–	$(9.5^{+4.9}_{-5.5})\times10^{-9}$
$k_\mathrm{B}T^{bb}(\mathrm{keV})$	$0.82^{+0.09}_{-0.06}$	–	–	$0.97^{+0.08}_{-0.05}$
$K_{dbb}(10^{16}\,\mathrm{m}^2)$	–	$(7^{+11}_{-4})\times10^{-4}$	$(1.2^{+1.2}_{-0.5})\times10^{-6}$	–
$k_\mathrm{B}T^{dbb}(\mathrm{keV})$	–	0.18 ± 0.01	0.40 ± 0.02	–
$K_{com}(10^{44}\,\mathrm{ph\,s^{-1}\,keV^{-1}})$	–	110^{+110}_{-40}	$4.8^{+2.9}_{-1.7}$	–
$k_\mathrm{B}T_0^{com}(\mathrm{keV})$	–	0.37 ± 0.01	0.47 ± 0.02	–
$k_\mathrm{B}T_1^{com}(\mathrm{keV})$	–	2.3 ± 0.1	$9.0^{+0.9}_{-0.7}$	–
τ^{com}	–	6.3 ± 0.2	$3.1^{+0.5}_{-0.7}$	–
$K_{pow}(10^{44}\,\mathrm{ph\,s^{-1}\,keV^{-1}})$	$0.13^{+0.39}_{-0.11}$	–	–	$2.4^{+1.6}_{-1.0}$
Γ^{pow}	$-0.33^{+0.74}_{-0.68}$	–	–	$0.94^{+0.27}_{-0.37}$
$N_H^{cold}(10^{22}\,\mathrm{cm^{-2}})$	2.0 ± 0.2	$1.05^{+0.04}_{-0.03}$	2.9 ± 0.1	4.57 ± 0.03
$N_H^{hot}(10^{20}\,\mathrm{cm^{-2}})$	100^{+40}_{-30}	$0.8^{+1.8}_{-0.3}$	$3.2^{+1.3}_{-1.2}$	20^{+11}_{-9}
$k_\mathrm{B}T^{hot}(\mathrm{keV})$	1.1 ± 0.2	$0.72^{+0.29}_{-0.12}$	1.0 ± 0.2	$0.91^{+0.29}_{-0.17}$
$zv^{hot}(\mathrm{km\,s^{-1}})$	>-129	>-114	>-108	>-104
$N_H^{xabs}(10^{22}\,\mathrm{cm^{-2}})$	$0.76^{+0.37}_{-0.29}$	98^{+5}_{-7}	–	–
$\log[\xi]^{xabs}(10^{-9}\,\mathrm{W\,m})$	2.4 ± 0.2	5.5 ± 0.1	–	–
$zv^{xabs}(10^2\,\mathrm{km\,s^{-1}})$	-32 ± 1	-8.5 ± 1.8	–	–
$K^{gauss1}(10^{44}\,\mathrm{ph\,s^{-1}})$	$0.16^{+0.02}_{-0.01}$	$1.3^{+0.1}_{-0.2}$	0.36 ± 0.02	–
$E^{gauss1}(\mathrm{keV})$	2.33 ± 0.01	2.26 ± 0.07	2.29 ± 0.04	–
$FWHM^{gauss1}(\mathrm{keV})$	0.38 ± 0.04	0.29 ± 0.02	0.27 ± 0.01	–
$K^{gauss2}(10^{44}\,\mathrm{ph\,s^{-1}})$	–	$3.3^{+0.9}_{-0.8}$	–	–
$E^{gauss2}(\mathrm{keV})$	–	3.4 ± 0.1	–	–
$FWHM^{gauss2}(\mathrm{keV})$	–	1.2 ± 0.1	–	–
$K^{gauss3}(10^{44}\,\mathrm{ph\,s^{-1}})$	–	$1.4^{+0.6}_{-0.5}$	–	–
$E^{gauss3}(\mathrm{keV})$	–	2.83 ± 0.02	–	–
$FWHM^{gauss3}(\mathrm{keV})$	–	$0.52^{+0.08}_{-0.09}$	–	–
C-stat/d.o.f	289/267	847/735	1058/710	877/844

NOTE.– K^i is the normalization of the i-th component, T the temperature for the (disk) black body, T_0 the average temperature of the seed photon, T_1 the average temperature of the output photon, τ the optical depth of the plasma, N_H^i the column density of the i-th component, T^{Hot} the temperature of the hot absorbing gas, zv^i the outflow velocity of the i-th component, $\log[\xi]$ the ionization parameter, E^i the energy of the i-th Gaussian, and $FWHM^i$ the Full-Width-Half-Maximum of the i-th Gaussian

TABLE A2
Best-fit data for 4U 1811-17, 4U 1642-45 & GX 5-1

	4U 1811-17	4U 1642-45	GX 5-1
Distance (kpc)	7	11	8.5
$K^{dbb}(10^{16}\,\mathrm{m}^2)$	$(3.2^{+1.0}_{-0.8})\times10^{-7}$	$(4.3^{+1.1}_{-0.8})\times10^{-3}$	$(3.1^{+3.9}_{-1.7})\times10^{-4}$
$k_\mathrm{B}T^{dbb}$(keV)	0.63 ± 0.02	0.27 ± 0.01	0.35 ± 0.02
$K_{com}(10^{44}\,\mathrm{ph\,s^{-1}\,keV^{-1}})$	35^{+51}_{-18}	153^{+3}_{-4}	740^{+70}_{-50}
$k_\mathrm{B}T_0^{com}$(keV)	0.84 ± 0.01	0.80 ± 0.01	$0.45^{+0.04}_{-0.03}$
$k_\mathrm{B}T_1^{com}$(keV)	$4.7^{+0.4}_{-0.3}$	4.1 ± 0.1	1.5 ± 0.1
τ^{com}	$2.6^{+1.2}_{-1.1}$	$3.1^{+0.1}_{-0.3}$	10.2 ± 0.3
$N_H^{cold}(10^{22}\,\mathrm{cm}^{-2})$	2.9 ± 0.1	$6.22^{+0.02}_{-0.04}$	4.1 ± 0.2
$N_H^{hot}(10^{20}\,\mathrm{cm}^{-2})$	$0.93^{+0.40}_{-0.62}$	<3.0	$4.3^{+1.0}_{-1.3}$
$k_\mathrm{B}T^{hot}$(keV)	$0.39^{+0.50}_{-0.20}$	$1.1^{+0.4}_{-0.3}$	$0.76^{+0.10}_{-0.15}$
$zv^{hot}(\mathrm{km\,s^{-1}})$	>58.5	>-385	-200^{+80}_{-100}
$N_H^{xabs}(10^{22}\,\mathrm{cm}^{-2})$	23 ± 5	$(5.6\pm1.4)\times10^{-2}$	$(5.1^{+1.8}_{-2.0})\times10^{-2}$
$\log[\xi]^{xabs}(10^{-9}\,\mathrm{W\,m})$	4.5 ± 0.1	2.6 ± 0.1	2.9 ± 0.1
$zv^{xabs}(10^2\,\mathrm{km\,s^{-1}})$	-3.2 ± 0.4	-9.7 ± 1.0	-16 ± 1
$K^{gauss1}(10^{44}\,\mathrm{ph\,s^{-1}})$	1.8 ± 0.1	$(5.7^{+2.2}_{-2.3})\times10^{-2}$	$6.8^{+0.7}_{-0.6}$
E^{gauss1}(keV)	2.28 ± 0.01	6.42 ± 0.01	2.23 ± 0.01
$FWHM^{gauss1}$(keV)	0.26 ± 0.01	$<3.7\times10^{-2}$	0.29 ± 0.02
$K^{gauss2}(10^{44}\,\mathrm{ph\,s^{-1}})$	$0.57^{+0.09}_{-0.08}$	$6.1^{+0.4}_{-0.3}$	–
E^{gauss2}(keV)	$2.63^{+0.01}_{-0.02}$	2.29 ± 0.01	–
$FWHM^{gauss2}$(keV)	$0.28^{+0.04}_{-0.03}$	0.26 ± 0.01	–
C-stat/d.o.f	1031/702	960/677	1278/907

NOTE.– Same caption as in Table A1

TABLE A3
Best-fit data for 4U 1624-49

Distance (kpc)	15		
$K^{bb}(10^{16}\,\mathrm{m}^2)$	$(6.9^{+3.3}_{-2.0})\times10^{-3}$	$(6.8^{+3.2}_{-1.9})\times10^{-3}$	$(6.8^{+3.3}_{-1.9})\times10^{-3}$
$k_\mathrm{B}T^{bb}$(keV)	0.18 ± 0.01	0.18 ± 0.01	0.18 ± 0.01
$K_{pow}(10^{44}\,\mathrm{ph\,s^{-1}\,keV^{-1}})$	340^{+80}_{-30}	340^{+110}_{-30}	340^{+350}_{-30}
Γ^{pow}	$2.09^{+0.03}_{-0.02}$	2.09 ± 0.03	$2.09^{+0.03}_{-0.02}$
$N_H^{cold}(10^{22}\,\mathrm{cm}^{-2})$	13.1 ± 0.2	13.1 ± 0.2	13.1 ± 0.2
$N_H^{hot}(10^{20}\,\mathrm{cm}^{-2})$	<6.3	<12	<22
$k_\mathrm{B}T^{hot}$(keV)	1.0 (fixed)	1.4 (fixed)	1.9 (fixed)
$zv^{hot}(\mathrm{km\,s^{-1}})$	0.0 (fixed)	0.0 (fixed)	0.0 (fixed)
$N_H^{xabs1}(10^{22}\,\mathrm{cm}^{-2})$	25^{+24}_{-9}	24^{+27}_{-8}	24^{+23}_{-8}
$\log[\xi]^{xabs1}(10^{-9}\,\mathrm{W\,m})$	$4.5^{+0.2}_{-0.1}$	$4.5^{+0.2}_{-0.1}$	$4.5^{+0.2}_{-0.1}$
$zv^{xabs1}(10^2\,\mathrm{km\,s^{-1}})$	$-3.4^{+1.3}_{-1.1}$	$-3.4^{+1.2}_{-1.1}$	$-3.4^{+1.3}_{-1.0}$
$N_H^{xabs2}(10^{22}\,\mathrm{cm}^{-2})$	$0.20^{+0.13}_{-0.10}$	$0.20^{+0.13}_{-0.10}$	$0.22^{+0.12}_{-0.11}$
$\log[\xi]^{xabs2}(10^{-9}\,\mathrm{W\,m})$	$2.3^{+0.2}_{-0.3}$	$2.3^{+0.2}_{-0.3}$	2.3 ± 0.3
$zv^{xabs2}(10^2\,\mathrm{km\,s^{-1}})$	$-9.1^{+5.0}_{-2.0}$	$-9.1^{+5.0}_{-2.0}$	$-9.0^{+5.5}_{-2.1}$
C-stat/d.o.f	514/520		

NOTE.– Same caption as in Table A1

TABLE A4
Best-fit data for 4U 1630-47

Distance (kpc)	10		
$K^{dbb}(10^{16}\,\mathrm{m}^2)$	$6.4^{+4.0}_{-2.7}$	$6.1^{+4.0}_{-2.4}$	$6.1^{+3.9}_{-2.4}$
$k_\mathrm{B}T^{dbb}(\mathrm{keV})$	0.18 ± 0.01	0.18 ± 0.01	0.18 ± 0.01
$K^{com}(10^{44}\,\mathrm{ph\,s^{-1}\,keV^{-1}})$	270^{+180}_{-30}	270^{+20}_{-40}	270^{+240}_{-100}
$k_\mathrm{B}T_0^{com}(\mathrm{keV})$	$0.78^{+0.01}_{-0.20}$	$0.78^{+0.01}_{-0.33}$	$0.78^{+0.01}_{-0.29}$
$k_\mathrm{B}T_1^{com}(\mathrm{keV})$	$2.0^{+1.8}_{-0.2}$	$2.0^{+0.9}_{-0.2}$	$2.0^{+0.4}_{-0.2}$
τ^{com}	$4.3^{+1.3}_{-1.1}$	$4.3^{+0.9}_{-1.4}$	$4.3^{+1.6}_{-1.4}$
$N_H^{cold}(10^{22}\,\mathrm{cm}^{-2})$	8.0 ± 0.1	8.0 ± 0.1	8.0 ± 0.1
$N_H^{hot}(10^{20}\,\mathrm{cm}^{-2})$	< 22	< 55	< 81
$k_\mathrm{B}T^{hot}(\mathrm{keV})$	1.0 (fixed)	1.4 (fixed)	1.9 (fixed)
$zv^{hot}(\mathrm{km\,s^{-1}})$	0.0 (fixed)	0.0 (fixed)	0.0 (fixed)
$N_H^{xabs}(10^{22}\,\mathrm{cm}^{-2})$	24^{+226}_{-12}	24^{+221}_{-12}	24^{+9}_{-14}
$\log[\xi]^{xabs}(10^{-9}\,\mathrm{W\,m})$	5.2 ± 0.1	5.2 ± 0.1	5.2 ± 0.1
$zv^{xabs}(10^2\,\mathrm{km\,s^{-1}})$	$-8.5^{+3.4}_{-2.6}$	$-8.7^{+3.6}_{-2.3}$	$-8.7^{+3.5}_{-2.4}$
$K^{gauss1}(10^{44}\,\mathrm{ph\,s^{-1}})$	7.0 ± 0.5	$7.0^{+5.2}_{-0.4}$	$6.9^{+0.5}_{-0.4}$
$E^{gauss1}(\mathrm{keV})$	2.262 ± 0.003	2.262 ± 0.003	2.262 ± 0.003
$FWHM^{gauss1}(\mathrm{keV})$	0.24 ± 0.01	0.24 ± 0.01	0.24 ± 0.01
$K^{gauss2}(10^{44}\,\mathrm{ph\,s^{-1}})$	$(5.1^{+1.2}_{-1.6}) \times 10^{-2}$	$(4.9^{+1.3}_{-1.4}) \times 10^{-2}$	$(4.9^{+1.4}_{-1.3}) \times 10^{-2}$
$E^{gauss2}(\mathrm{keV})$	3.171 ± 0.002	3.172 ± 0.002	3.172 ± 0.002
$FWHM^{gauss2}(\mathrm{keV})$	$< 2.4 \times 10^{-2}$	$< 2.4 \times 10^{-2}$	$< 2.6 \times 10^{-2}$
C-stat/d.o.f	1203/515		

NOTE.– Same caption as in Table A1

TABLE A5
Best-fit data for 4U 1702-429

Distance (kpc)	5.5		
$K^{dbb}(10^{16}\,\mathrm{m}^2)$	$(2.4^{+2.0}_{-0.9}) \times 10^{-9}$	$(2.6^{+2.1}_{-0.9}) \times 10^{-9}$	$(2.6^{+2.0}_{-1.0}) \times 10^{-9}$
$k_\mathrm{B}T^{dbb}(\mathrm{keV})$	$0.91^{+0.09}_{-0.12}$	$0.89^{+0.10}_{-0.08}$	$0.90^{+0.09}_{-0.06}$
$K^{com}(10^{44}\,\mathrm{ph\,s^{-1}\,keV^{-1}})$	$5.7^{+0.9}_{-0.7}$	$5.7^{+1.0}_{-0.7}$	5.7 ± 0.7
$k_\mathrm{B}T_0^{com}(\mathrm{keV})$	$0.20^{+0.02}_{-0.03}$	0.20 ± 0.03	$0.20^{+0.02}_{-0.03}$
$k_\mathrm{B}T_1^{com}(\mathrm{keV})$	$2.9^{+0.5}_{-0.3}$	$2.9^{+0.5}_{-0.3}$	$2.9^{+0.4}_{-0.3}$
τ^{com}	$6.4^{+0.7}_{-0.9}$	$6.3^{+0.9}_{-0.6}$	$6.3^{+0.8}_{-0.7}$
$N_H^{cold}(10^{22}\,\mathrm{cm}^{-2})$	2.0 ± 0.1	2.0 ± 0.1	2.0 ± 0.1
$N_H^{hot}(10^{20}\,\mathrm{cm}^{-2})$	< 1.2	< 1.2	< 1.4
$k_\mathrm{B}T^{hot}(\mathrm{keV})$	1.0 (fixed)	1.4 (fixed)	1.9 (fixed)
$zv^{hot}(\mathrm{km\,s^{-1}})$	0.0 (fixed)	0.0 (fixed)	0.0 (fixed)
$N_H^{xabs}(10^{22}\,\mathrm{cm}^{-2})$	$(1.7^{+1.1}_{-0.9}) \times 10^{-2}$	$(1.6^{+1.2}_{-0.8}) \times 10^{-2}$	$(1.6^{+1.2}_{-0.9}) \times 10^{-2}$
$\log[\xi]^{xabs}(10^{-9}\,\mathrm{W\,m})$	2.3 ± 0.2	2.3 ± 0.2	2.3 ± 0.2
$zv^{xabs}(10^2\,\mathrm{km\,s^{-1}})$	$-4.9^{+2.5}_{-2.6}$	$-4.9^{+2.6}_{-2.5}$	$-4.8^{+2.6}_{-2.5}$
C-stat/d.o.f	1003/1004		

NOTE.– Same caption as in Table A1

TABLE A6
Best-fit data for 1E 1740.7-2942

Distance (kpc)	8.5		
$K^{bb}(10^{16}\,\mathrm{m}^2)$	$(2.6^{+2.2}_{-2.0})\times10^{-9}$	$(2.6\pm2.0)\times10^{-9}$	$(2.7^{+2.3}_{-2.1})\times10^{-9}$
$k_{\mathrm{B}}T^{bb}(\mathrm{keV})$	$1.4^{+0.7}_{-0.2}$	$1.4^{+0.8}_{-0.2}$	$1.4^{+0.8}_{-0.2}$
$K^{pow}(10^{44}\,\mathrm{ph\,s^{-1}\,keV^{-1}})$	$0.7^{+1.2}_{-0.7}$	$0.7^{+1.3}_{-0.7}$	$0.7^{+1.3}_{-0.7}$
Γ^{pow}	$0.7^{+2.4}_{-0.6}$	$0.7^{+2.1}_{-0.6}$	$0.7^{+2.2}_{-0.6}$
$N_H^{cold}(10^{22}\,\mathrm{cm}^{-2})$	14^{+2}_{-1}	14^{+2}_{-1}	14^{+2}_{-1}
$N_H^{hot}(10^{20}\,\mathrm{cm}^{-2})$	<16	<22	<35
$k_{\mathrm{B}}T^{hot}(\mathrm{keV})$	1.0(fixed)	1.4(fixed)	1.9(fixed)
$zv^{hot}(\mathrm{km\,s^{-1}})$	0.0(fixed)	0.0(fixed)	0.0(fixed)
C-stat/d.o.f	413/407		

NOTE.– Same caption as in Table A1

TABLE A7
Best-fit data for SAX J1747.0-2853

Distance (kpc)	7.5		
$K^{bb}(10^{16}\,\mathrm{m}^2)$	$(8.0^{+7.8}_{-3.0})\times10^{-9}$	$(8.0^{+7.2}_{-4.2})\times10^{-9}$	$(8.0^{+7.3}_{-3.1})\times10^{-9}$
$k_{\mathrm{B}}T^{bb}(\mathrm{keV})$	$0.92^{+0.11}_{-0.04}$	$0.92^{+0.09}_{-0.05}$	$0.92^{+0.22}_{-0.05}$
$K^{pow}(10^{44}\,\mathrm{ph\,s^{-1}\,keV^{-1}})$	$0.6^{+2.0}_{-0.3}$	$0.6^{+2.1}_{-0.1}$	$0.6^{+1.7}_{-0.1}$
Γ^{pow}	$0.81^{+0.24}_{-0.38}$	$0.81^{+0.12}_{-0.60}$	$0.81^{+0.89}_{-0.63}$
$N_H^{cold}(10^{22}\,\mathrm{cm}^{-2})$	$9.0^{+1.3}_{-0.7}$	$9.0^{+1.3}_{-0.7}$	$9.0^{+1.2}_{-0.7}$
$N_H^{hot}(10^{20}\,\mathrm{cm}^{-2})$	<1.4	<1.8	<3.0
$k_{\mathrm{B}}T^{hot}(\mathrm{keV})$	1.0 (fixed)	1.4 (fixed)	1.9 (fixed)
$zv^{hot}(\mathrm{km\,s^{-1}})$	0.0 (fixed)	0.0 (fixed)	0.0 (fixed)
$N_H^{xabs}(10^{22}\,\mathrm{cm}^{-2})$	14^{+116}_{-13}	14^{+56}_{-13}	14^{+79}_{-13}
$\log[\xi]^{xabs}(10^{-9}\,\mathrm{W\,m})$	$4.0^{+0.7}_{-1.0}$	$4.0^{+0.7}_{-1.1}$	$4.0^{+0.6}_{-1.1}$
$zv^{xabs}(10^2\,\mathrm{km\,s^{-1}})$	-18^{+2}_{-3}	-18^{+2}_{-3}	-18^{+2}_{-3}
C-stat/d.o.f	527/553		

NOTE.– Same caption as in Table A1

References

[1] Tielens, A. G. G. M., *The Physics and Chemistry of the Interstellar Medium*, Cambridge University Press, 2005.

[2] Ferrière, K. M., *The interstellar environment of our galaxy*, Reviews of Modern Physics, **vol. 73**, pp. 1031–1066, 2001.

[3] Wang, Q. D., *Global Hot Gas in and around the Galaxy*, in *American Institute of Physics Conference Series*, edited by Smith, R. K., Snowden, S. L., and Kuntz, K. D., American Institute of Physics Conference Series, **vol. 1156**, pp. 257–267, 2009.

[4] Gatto, A., Walch, S., Low, M.-M. M., Naab, T., Girichidis, P., Glover, S. C. O., Wünsch, R., Klessen, R. S., Clark, P. C., Baczynski, C., Peters, T., Ostriker, J. P., Ibáñez-Mejía, J. C., and Haid, S., *Modelling the supernova-driven ISM in different environments*, Monthly Notices of the Royal Astronomical Society, **vol. 449**, pp. 1057–1075, 2015.

[5] Yao, Y., and Wang, Q. D., *X-Ray Absorption Line Spectroscopy of the Galactic Hot Interstellar Medium*, The Astrophysical Journal, **vol. 624**, pp. 751–764, 2005.

[6] Yao, Y., and Wang, Q. D., *The Galactic Central Diffuse X-Ray Enhancement: A Differential Absorption/Emission Analysis*, The Astrophysical Journal, **vol. 666**, pp. 242–246, 2007.

[7] Yao, Y., and Wang, Q. D., *X-Ray Absorption Spectroscopy of the Multiphase Interstellar Medium: Oxygen and Neon Abundances*, The Astrophysical Journal, **vol. 641**, pp. 930–937, 2006.

[8] Wang, Q. D., *Chandra Observations of the Galactic Center: High Energy Processes at Arcsecond Resolution*, Journal of Physics Conference Series, **vol. 54**, pp. 115–125, 2006.

[9] Wang, Q. D., Nowak, M. A., Markoff, S. B., Baganoff, F. K., Nayakshin, S., Yuan, F., Cuadra, J., Davis, J., Dexter, J., Fabian, A. C., Grosso, N., Haggard, D., Houck, J., Ji, L., Li, Z., Neilsen, J., Porquet, D., Ripple, F., and Shcherbakov, R. V., *Dissecting X-ray-Emitting Gas Around the Center of Our Galaxy*, Science, **vol. 341**, pp. 981–983, 2013.

[10] van Paradijs, J., and McClintock, J. E., *Optical and ultraviolet observations of X-ray binaries.*, X-ray Binaries, pp. 58–125, 1995.

[11] Eggleton, P. P., *Approximations to the radii of Roche lobes*, The Astrophysical Journal, **vol. 268**, p. 368, 1983.

[12] King, A., *Accretion in close binaries.*, X-ray Binaries, pp. 419–456, 1995.

[13] Padmanabhan, T., *Theoretical Astrophysics - Volume 1, Astrophysical Processes*, Cambridge University Press, 2000.

[14] Boirin, L., Parmar, A. N., Barret, D., Paltani, S., and Grindlay, J. E., *Discovery of X-ray absorption features from the dipping low-mass X-ray binary XB 1916-053 with XMM-Newton*, Astronomy and Astrophysics, **vol. 418**, pp. 1061–1072, 2004.

[15] Mewe, R., *Atomic Physics of Hot Plasmas*, in *X-Ray Spectroscopy in Astrophysics*, edited by van Paradijs, J., and Bleeker, J. A. M., Lecture Notes in Physics, Berlin Springer Verlag, **vol. 520**, pp. 109–188, 1999.

[16] Boirin, L., Méndez, M., Díaz Trigo, M., Parmar, A. N., and Kaastra, J. S., *A highly-ionized absorber in the X-ray binary 4U 1323-62: A new explanation for the dipping phenomenon*, Astronomy and Astrophysics, **vol. 436**, pp. 195–208, 2005.

[17] Lei, Y.-J., Zhang, S., Qu, J.-L., Yuan, H.-L., Wang, Y.-N., Dong, Y.-Q., Zhang, H.-T., Li, Z.-B., Zhang, C.-M., and Zhao, Y.-H., *The Properties of Cross-correlation and Spectra of the Low-mass X-Ray Binary 4U 1608-52*, The Astronomical Journal, **vol. 147**, 67, 2014.

[18] Iaria, R., Lavagetto, G., D'Aí, A., di Salvo, T., and Robba, N. R., *Chandra observation of the Big Dipper X 1624-490*, Astronomy and Astrophysics, **vol. 463**, pp. 289–295, 2007.

[19] Díaz Trigo, M., Migliari, S., Miller-Jones, J. C. A., and Guainazzi, M., *XMM-Newton observations reveal the disappearance of the wind in 4U 1630-47*, Astronomy and Astrophysics, **vol. 571**, A76, 2014.

[20] Zhang, G., Méndez, M., Zamfir, M., and Cumming, A., *The link between coherent burst oscillations, burst spectral evolution and accretion state in 4U 1728-34*, Monthly Notices of the Royal Astronomical Society, **vol. 455**, pp. 2004–2017, 2016.

[21] Paizis, A., Ebisawa, K., Takahashi, H., Dotani, T., Kohmura, T., Kokubun, M., Rodriguez, J., Ueda, Y., Walter, R., Yamada, S., Yamaoka, K., and Yuasa, T., *Broad-Band Spectrum of the Black Hole Candidate IGR J17497-2821 Studied with Suzaku*, Publications of the Astronomical Society of Japan, **vol. 61**, pp. S107–S113, 2009.

[22] D'Aì, A., Iaria, R., Di Salvo, T., Riggio, A., Burderi, L., and Robba, N. R., *Chandra X-ray spectroscopy of a clear dip in GX 13+1*, Astronomy and Astrophysics, **vol. 564**, A62, 2014.

[23] Fender, R. P., and Hendry, M. A., *The radio luminosity of persistent X-ray binaries*, Monthly Notices of the Royal Astronomical Society, **vol. 317**, pp. 1–8, 2000.

[24] Galloway, D. K., Muno, M. P., Hartman, J. M., Psaltis, D., and Chakrabarty, D., *Thermonuclear (Type I) X-Ray Bursts Observed by the Rossi X-Ray Timing Explorer*, The Astrophysical Journal Supplement Series, **vol. 179**, pp. 360–422, 2008.

[25] Natalucci, L., Tomsick, J. A., Bazzano, A., Smith, D. M., Bachetti, M., Barret, D., Boggs, S. E., Christensen, F. E., Craig, W. W., Fiocchi, M., Fürst, F., Grefenstette, B. W., Hailey, C. J., Harrison, F. A., Krivonos, R., Kuulkers, E., Miller, J. M., Pottschmidt, K., Stern, D., Ubertini, P., Walton, D. J., and Zhang, W. W., *NuSTAR and INTEGRAL Observations of a Low/Hard State of 1E1740.7-2942*, The Astrophysical Journal, **vol. 780**, p. 63, 2014.

[26] Werner, N., in't Zand, J. J. M., Natalucci, L., Markwardt, C. B., Cornelisse, R., Bazzano, A., Cocchi, M., Heise, J., and Ubertini, P., *X-ray spectral evolution of SAX J1747.0-2853 during outburst activity and confirmation of its transient nature*, Astronomy and Astrophysics, **vol. 416**, pp. 311–318, 2004.

[27] Smith, R. K., Dame, T. M., Costantini, E., and Predehl, P., *The X-Ray Halo of GX 5-1*, The Astrophysical Journal, **vol. 648**, pp. 452–460, 2006.

[28] Markert, T. H., Canizares, C. R., Dewey, D., McGuirk, M., Pak, C. S., and Schattenburg, M. L., *High-Energy Transmission Grating Spectrometer for the Advanced X-ray Astrophysics Facility (AXAF)*, in *EUV, X-Ray, and Gamma-Ray Instrumentation for Astronomy V*, edited by Siegmund, O. H., and Vallerga, J. V., Society of Photo-Optical Instrumentation Engineers (SPIE) Conference Series, **vol. 2280**, pp. 168–180, 1994.

[29] Díaz Trigo, M., Parmar, A. N., Boirin, L., Méndez, M., and Kaastra, J. S., *Spectral changes during dipping in low-mass X-ray binaries due to highly-ionized absorbers*, Astronomy and Astrophysics, **vol. 445**, pp. 179–195, 2006.

[30] Miller, J. M., Fabian, A. C., Wijnands, R., Remillard, R. A., Wojdowski, P., Schulz, N. S., Di Matteo, T., Marshall, H. L., Canizares, C. R., Pooley, D., and Lewin, W. H. G., *Resolving the Composite Fe Kα Emission Line in the Galactic Black Hole Cygnus X-1 with Chandra*, The Astrophysical Journal, **vol. 578**, pp. 348–356, 2002.

[31] Cash, W., *Parameter estimation in astronomy through application of the likelihood ratio*, The Astrophysical Journal, **vol. 228**, pp. 939–947, 1979.

[32] Gillessen, S., Eisenhauer, F., Fritz, T. K., Pfuhl, O., Ott, T., and Genzel, R., *The distance to the Galactic Center*, in *IAU Symposium*, edited by de Grijs, R., IAU Symposium, **vol. 289**, pp. 29–35, 2013.

[33] Welsh, B. Y., and Shelton, R. L., *The trouble with the Local Bubble*, Astrophysics and Space Science, **vol. 323**, pp. 1–16, 2009.

[34] Vasiliev, E. O., Nath, B. B., and Shchekinov, Y., *Evolution of multiple supernova remnants*, Monthly Notices of the Royal Astronomical Society, **vol. 446**, pp. 1703–1715, 2015.

[35] Costantini, E., *The Ultraviolet-X-Ray Connection in AGN Outflows*, Space Science Reviews, **vol. 157**, pp. 265–277, 2010.